

Contrast Source Inversion-Enhanced Synthetic Aperture Approach for Microwave Multilayered Subsurface Imaging

Yoshihiro Yamauchi and Shouhei Kidera[✉], *Senior Member, IEEE*

Abstract—This article presents an inverse scattering analysis-enhanced radar imaging method by incorporating synthetic aperture radar (SAR) and contrast source inversion (CSI) to enhance the imaging accuracy of a microwave ground-penetrating radar (GPR) model. The GPR SAR propagation model could be accurately determined via the CSI optimization output, i.e., the electric total fields of all region of interest (ROI) cells and observation areas, which generate an accurate Green's function as the propagation model in a heterogeneous background medium. Additionally, the scattered field, assuming a multilayered background, is reconstructed using a CSI scheme. Numerical tests based on the finite-difference time domain (FDTD) show that our proposed method considerably improves the reconstruction accuracy for target localization, even in highly heterogeneous multilayered background media.

Index Terms—Contrast source inversion method (CSI), ground-penetrating radar (GPR), inverse scattering, microwave subsurface imaging, synthetic aperture radar (SAR).

I. INTRODUCTION

RECENTLY, there has been a high demand for reliable underground monitoring techniques because water or air cavity buried in the ground could cause catastrophic collapses [1]. Microwave ground-penetrating radar (GPR) is among most promising underground monitoring tools owing to its deeper penetration depth into the ground at the meter scale using lower frequency bands, such as under 1 GHz. The GPR is also promising for various monitoring techniques, such as the nondestructive inspection of infrastructures, (e.g., roads or bridges), and the exploration of oil, minerals, and water resources [2], [3]. In addition, effective monitoring by the GPR addresses problem where highly efficient and wide-area surveys are required, such as water leakages due to aging infrastructure in water and sewage systems or road collapses caused by the excavation of underground tunnels.

Manuscript received 11 January 2023; revised 14 May 2023; accepted 14 July 2023. Date of publication 1 August 2023; date of current version 6 September 2023. This work was supported in part by the Japan Science and Technology Agency (JST) Fusion Oriented REsearch for disruptive Science and Technology (FOREST) Program, Japan, under Grant JPMJFR2025; and in part by the commissioned research of "National Institute for Land and Infrastructure Management," under technology research and development system of "The Committee on Advanced Road Technology" established by the Ministry of Land, Infrastructure, Transport and Tourism (MLIT), Japan. (Corresponding author: Shouhei Kidera.)

The authors are with the Graduate School of Informatics and Engineering, The University of Electro-Communications, Tokyo 182-8585, Japan (e-mail: kidera@uec.ac.jp).

Color versions of one or more figures in this article are available at <https://doi.org/10.1109/TAP.2023.3298971>.

Digital Object Identifier 10.1109/TAP.2023.3298971

The main imaging approach used in GPR operations is synthetic aperture radar (SAR), which offers a high spatial resolution through antenna scanning and reflectivity coefficient profile reconstruction [4], [5], [6]. In addition, a sparse regularization approach is used to address the limited data volume [7], [8]. Nevertheless, it is generally challenging to retrieve the dielectric properties of underground objects, such as air, water-filled materials, and metallic objects, from such qualitative radar images. Thus, the radar-based approach requires an accurate propagation model from background media. However, because a single homogeneous medium is adopted as the propagation model in most cases, there are non-negligible errors in reconstructing the position or shape of an object when dealing with heterogeneous background media, such as multilayer structures, which are usually considered in real underground structures. While certain techniques for stratified media exist, such as [6], the majority of them do not account for the multiple scattering effects among layers or signal attenuation owing to lossy medium.

The other approach in the GPR operations is nonlinear inverse scattering (NIS) analysis by solving the domain integral equation. While the NIS approach can quantitatively provide a spatial profile of complex permittivity, the above-mentioned inverse problem is nonlinear and usually requires massive computational costs, particularly in the 3-D model. Therefore, various NIS methods have been developed, such as Born approximation [9], [10] with extensions to the GRP model [11], [12], [13], and contrast source inversion (CSI) [14], [15], [16]. There are some efficient approaches, assuming a GPR scenario, such as multi-resolution techniques, [17], [18], [19], [20], [21] or Bayesian compressed sensing [17], [22], [23], [24], which improve dielectric property reconstruction accuracy by significantly reducing the number of unknowns or sparse regularization to counteract the ill-posedness. The CSI approach can reduce computational costs to avoid the iterative use of forward solvers, such as finite-difference time-domain (FDTD), by simultaneously optimizing the contrast function and total field. Further, using the CSI approach has been studied extensively for the GPR or subsurface observation model [25], [26], [27], [28]. However, it has an inherent problem: the number of data samples is considerably less than that of unknowns. The ill-posed condition causes a severe dependency in the initial estimation in the optimization problem. This ill-posed feature would be severe in the general GPR model because an illumination

angle would be considerably limited. To resolve the above mentioned ill-posed problems, some approaches using the radar-based region of interest (ROI) limitation have been developed [29], [30], [31], [32], [33], [34], where an ROI is allocated only to the existing area of an object. Various studies have demonstrated that these approaches drastically reduce the number of unknowns and enhance the reconstruction accuracy of the complex permittivity profile. However, the propagation model assuming a homogeneous medium would produce severe inaccuracy in providing a target shape or location, (i.e., the ROI), in the case of a heterogeneous background, such as a multilayered ground structure.

Some studies have tried to generate an accurate radar image assuming multilayered background by modifying Green's function [35]. However, this approach requires several impractical assumptions, such as completely clutter suppressed signals, prior knowledge of relative permittivity for each layer, and ignoring the multipath reflections. To address the above issue, we introduce a method to generate CSI-based propagation model for accurate radar imaging even in heterogeneous background media. In the proposed method, we focus on the notable features of CSI, such as its ability to provide the contrast function of the dielectric property, and all the total fields in the observation and ROI areas. These outputs enable us to estimate Green's function in propagating from the transmitter to the object and from the object to the receiver. Thus, the CSI approach can provide an accurate propagation model. Furthermore, the proposed method can precisely estimate the total field responses for multilayered background media by exploiting the above CSI outputs. This exploitation is necessary to reconstruct the profile of an underground object by eliminating other clutter components, such as multi-reflection among layers. While the fundamental study for this method has been reported in [36] in the breast tumor detection issue, it requires some impractical assumptions that a permittivity profile of background media (breast without tumor) is known, and the subtraction signals between the case with and without tumor are accurately provided.

To maintain sufficient accuracy in the CSI results, we introduced a reduction scheme for unknowns, where multiple layers with homogeneity are assumed [37], and the basic idea has been also introduced in [38]; however, it only assumes a case that a dielectric property of each layer is completely given. Thus, the main contributions of this study are as follows.

- 1) The CSI-based inverse scattering approach is used to estimate an appropriate propagation model in the SAR method. The optimized total field within the ROI facilitates an accurate evaluation of the Green's function. Further, it generates background clutter due to multilayered media, which can suppress a false image resulting from the reflections between the layers.
- 2) The object buried in the multilayered background can be accurately reconstructed by exploiting the above Green's function and by eliminating a clutter response generated by the outputs of the CSI optimization process.
- 3) Minimizing the CSI cost function, the initial estimations of complex permittivity for multilayered background (three-layered ground) are efficiently reconstructed.

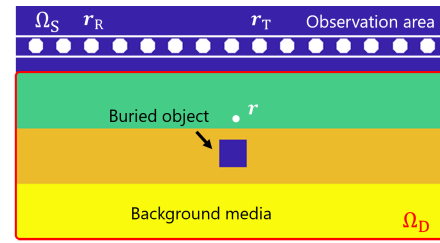


Fig. 1. Observation model. White solid circles denote locations of transmitter or receiver.

- 4) The proposed method substantially solves several significant problems in existing methods, that is, they require a prior knowledge for relative permittivity of each layer, an assumption of clutter free environment, a computationally expensive forward solver to generate the Green's function.

The numerical validations using the 2-D FDTD assuming a multilayered ground medium show that the proposed method retains a considerable advantage over the traditional SAR approaches.

II. OBSERVATION MODEL

Fig. 1 shows the observation model and array configurations in a 2-D model. In the model, several transmitters and receivers are arranged in a straight line along the y axis, with their locations denoted as \mathbf{r}_T and \mathbf{r}_R , respectively. The area where these sensors exist is defined as the domain Ω_S . A multilayered background medium with a planar structure is set before the above array. $E^T(\omega; \mathbf{r}_T, \mathbf{r}_R)$ is the total electric field recorded at the receiver \mathbf{r}_R , where the current source is induced at the transmitter \mathbf{r}_T . The multilayered background medium is placed in the air, with each layer having a homogeneous profile of complex permittivity. The scattered electric field at the angular frequency ω is defined as: $E^S(\omega; \mathbf{r}_T, \mathbf{r}_R) \equiv E^T(\omega; \mathbf{r}_T, \mathbf{r}_R) - E^I(\omega; \mathbf{r}_T, \mathbf{r}_R)$, where $E^I(\omega; \mathbf{r}_T, \mathbf{r}_R)$ is the incident electric field. Ω_D denotes the ROI.

III. TRADITIONAL METHODS

A. SAR Method

The SAR approach is the most prominent confocal radar imaging approach. Furthermore, the SAR imaging process has been widely introduced in far- and near-field observation scenarios, such as GPR applications. Among the many SAR-based inversion algorithms, the delay-and-sum (DAS) algorithm (i.e., backprojection algorithm) offers the most accurate radar images. In this case, the radar image $I(\mathbf{r})$ is calculated as follows:

$$I(\mathbf{r}) = \sum_{(\mathbf{r}_T, \mathbf{r}_R) \in \Omega_S} \int_{-\infty}^{\infty} E^S(\omega; \mathbf{r}_T, \mathbf{r}_R) \times G_R^{B*}(\omega; \mathbf{r}, \mathbf{r}_R) G_T^{B*}(\omega; \mathbf{r}_T, \mathbf{r}) d\omega \quad (1)$$

where $*$ denotes the complex conjugate, $G_T(\omega; \mathbf{r}_T, \mathbf{r})$ denotes the Green's function from the transmitter position \mathbf{r}_T to the imaging point \mathbf{r} , and $G_R(\omega; \mathbf{r}, \mathbf{r}_R)$ is the Green's function from

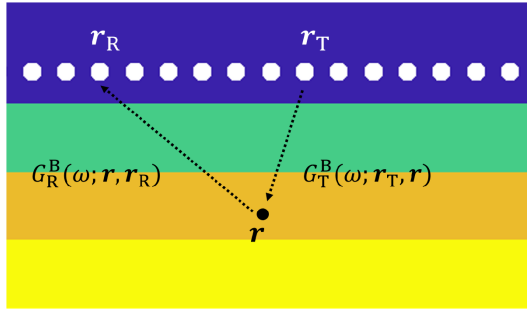


Fig. 2. Green's functions in SAR imaging in multilayer model.

the imaging point \mathbf{r} to the receiver position \mathbf{r}_R , the illustration of which is shown in Fig. 2.

Assuming a homogeneous background, which has been mainly adopted in studies [4] and [5], the above Green's functions are approximated as

$$G_T^B(\omega; \mathbf{r}_T, \mathbf{r}) \simeq \exp\left(j \frac{\omega}{c_B} \|\mathbf{r} - \mathbf{r}_T\|\right) \quad (2)$$

$$G_R^B(\omega; \mathbf{r}, \mathbf{r}_R) \simeq \exp\left(j \frac{\omega}{c_B} \|\mathbf{r}_R - \mathbf{r}\|\right). \quad (3)$$

Here c_B denotes the propagation speed of the assumed background medium, the ground medium. In most cases, the propagation speed of the background medium is constant; that is, a Single-layered homogeneous ground medium is assumed. However, an actual ground medium has a heterogeneous structure, (e.g., multilayered structure with different dielectric properties). The traditional SAR process produces non-negligible errors in estimating the position or shape of a buried object. Conversely, an accurate propagation model in a heterogeneous background is hardly available. An accurate forward solver, such as the FDTD approach, on the other hand, necessitates a high computing cost, as dielectric properties of antennas or other equipment must be accurately provided. Furthermore, it requires the complete suppression of clutter signals, which are caused by heterogeneous stratified media, i.e., multiple reflections among layers. Even if a prior knowledge of a number or thickness of layers are given, solely eliminating clutter signals from the received signals can be challenging, particular in the case of signals constituting reflections from layers at the same depth as the buried object.

B. Contrast Source Inversion

To overcome these issues, we focus on a distinct feature of the CSI method, one of the most promising inverse scattering algorithms [14]. Following the CSI method, the scattered electric field $E^S(\omega; \mathbf{r}_T, \mathbf{r}_R)$ is first formulated as the following domain integral equation:

$$E^S(\omega; \mathbf{r}_T, \mathbf{r}_R) = k_B^2 \int_{\Omega_D} G^B(\omega; \mathbf{r}, \mathbf{r}_R) w(\omega; \mathbf{r}_T, \mathbf{r}) d\mathbf{r}. \quad (4)$$

Here k_B and $G^B(\omega; \mathbf{r}, \mathbf{r}_R)$ denote the wavenumber and Green's function of the background media, respectively. $\chi(\omega; \mathbf{r}) \equiv (\epsilon(\mathbf{r}) - \epsilon_B(\mathbf{r})) / \epsilon_B(\mathbf{r})$ is defined as the contrast function, where $\epsilon(\mathbf{r})$ and $\epsilon_B(\mathbf{r})$ are complex permittivities at the position

\mathbf{r} with and without an object, respectively. $w(\omega; \mathbf{r}_T, \mathbf{r}) \equiv \chi(\omega; \mathbf{r}) E^T(\omega; \mathbf{r}_T, \mathbf{r})$ is the contrast source. The CSI method exploits the physical condition that (4) should hold not only at Ω_S but also at Ω_D , to introduce the following cost function:

$$\begin{aligned} F(\chi, w) &\equiv \frac{\sum_{\mathbf{r}_T} \|E^S(\omega; \mathbf{r}_T, \mathbf{r}_R) - \mathcal{G}^S[w]\|_{\Omega_S}^2}{\sum_{\mathbf{r}_T} \|E^S(\omega; \mathbf{r}_T, \mathbf{r}_R)\|_{\Omega_S}^2} \\ &+ \lambda \frac{\sum_{\mathbf{r}_T} \|\chi(\omega; \mathbf{r}) E^I(\omega; \mathbf{r}_T, \mathbf{r}') - w(\omega; \mathbf{r}_T, \mathbf{r}) + \chi(\omega; \mathbf{r}) \mathcal{G}^D[w]\|_{\Omega_D}^2}{\sum_{\mathbf{r}_T} \|\chi(\omega; \mathbf{r}) E^I(\omega; \mathbf{r}_T, \mathbf{r}')\|_{\Omega_D}^2} \end{aligned} \quad (5)$$

where λ denotes the regularization coefficient, and the operators \mathcal{G}^S and \mathcal{G}^D are defined as

$$\mathcal{G}^S[w] = k_B^2 \int_{\Omega_D} G^B(\omega; \mathbf{r}_R, \mathbf{r}) w(\omega; \mathbf{r}_T, \mathbf{r}) d\mathbf{r}, \quad (\mathbf{r}_R \in \Omega_S) \quad (6)$$

$$\mathcal{G}^D[w] = k_B^2 \int_{\Omega_D} G^B(\omega; \mathbf{r}', \mathbf{r}) w(\omega; \mathbf{r}_T, \mathbf{r}) d\mathbf{r}, \quad (\mathbf{r}' \in \Omega_D). \quad (7)$$

$\|\cdot\|_{\Omega_S}^2$ and $\|\cdot\|_{\Omega_D}^2$ denote the l_2 norms calculated in Ω_S and Ω_D , respectively. The CSI sequentially updates the three valuables, $w(\mathbf{r}_T, \mathbf{r})$, $E^T(\omega; \mathbf{r}_T, \mathbf{r})$, and $\chi(\omega; \mathbf{r})$ with $\mathbf{r} \in \Omega_D$ to minimize the cost function (5). The CSI considerably reduces the computational cost by avoiding an iterative use of the forward solver, because the total field $E^T(\omega; \mathbf{r}_T, \mathbf{r})$ in the ROI is optimized. This distinguishing feature of CSI is exploited in an extended SAR imaging scenario.

IV. PROPOSED METHOD

To address the problem of traditional SAR method, i.e., inaccuracy in the heterogeneous background, we propose a CSI-enhanced SAR method.

A. Initial Estimate of Multilayered Background Media

We first apply an initial estimate approach of relative permittivity in each layer of the background media. In the GPR observation model, the CSI method suffers from inaccuracy owing to a considerably higher number of unknowns than data samples. Thus, we introduce a reduction approach for unknowns below, considering a multilayered medium that assumes inversion of the terahertz band [37]. Reducing the number of unknowns assumes that each layer has a homogeneous medium with constant dielectric properties. First, the unknown set of vectors is defined as $\chi \equiv (\chi_1, \dots, \chi_n, \dots, \chi_{N_{\text{layer}}})$, where χ_n is the contrast function of the n th layer and N_{layer} is the number of layers. Second, the optimized combination vector $\hat{\chi}$ is determined as follows:

$$\hat{\chi} = \arg \min_{\chi} \sum_{n=1}^{N_{\text{layer}}} F(\chi_n, w_n; \Omega_{D,n}) \quad (8)$$

where w_n denotes the contrast source value of the n th layer, optimized in the CSI iteration with the initial set of χ , fixed in the iteration sequences. $F(\chi_n, w_n; \Omega_{D,n})$ expresses the cost function for the integral area of the n th layer as $\Omega_{D,n}$.

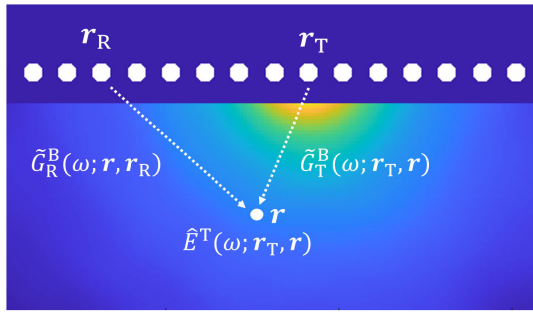


Fig. 3. Total electric field at the specific transmitter \mathbf{r}_T and the Green's functions optimized in the CSI scheme.

The original CSI should allocate a huge number of unknowns to a full region of several layers as ROI but this approach drastically decreases the number of unknowns to only n variables denoted as χ_n in the optimization. The above methodology and characteristics have been detailed in [37]. Furthermore, using the estimate of χ , the CSI procedure optimizes the total field in each ROI cell, defined as $\hat{E}^T(\omega; \mathbf{r}_T, \mathbf{r})$, which is then used in the post-SAR scheme detailed in Section IV-B.

B. CSI-Enhanced SAR

This section describes the enhanced SAR algorithm applied to unknown background heterogeneous media. By exploiting the initial estimate of the CSI described in Section IV-A, (i.e., the contrast function $\hat{\chi}$) and the total field in the ROI as $\hat{E}^T(\omega; \mathbf{r}_T, \mathbf{r})$, the Green's functions in (1) are modified as

$$\tilde{G}_T^B(\omega; \mathbf{r}_T, \mathbf{r}) \equiv \frac{\hat{E}^T(\omega; \mathbf{r}_T, \mathbf{r})}{E_{\text{air}}^T(\omega; \mathbf{r}_T, \mathbf{r}_T)} \quad (9)$$

$$\tilde{G}_R^B(\omega; \mathbf{r}_R, \mathbf{r}) \equiv \frac{\hat{E}^T(\omega; \mathbf{r}_R, \mathbf{r})}{E_{\text{air}}^T(\omega; \mathbf{r}_R, \mathbf{r}_R)}. \quad (10)$$

Here, $E_{\text{air}}^T(\omega; \mathbf{r}_T, \mathbf{r}_T)$ and $E_{\text{air}}^T(\omega; \mathbf{r}_R, \mathbf{r}_R)$ denote the total fields generated by the source located and observed at \mathbf{r}_T and \mathbf{r}_R , respectively, assuming the background media as vacuum. Fig. 3 shows the definition of each Green's function provided by the total field optimized by CSI. $\hat{E}^T(\omega; \mathbf{r}_T, \mathbf{r})$ and $\hat{E}^T(\omega; \mathbf{r}_R, \mathbf{r})$ are the total fields at $\mathbf{r} \in \Omega_D$ reconstructed following the CSI method described in Section IV-A, where $\chi(\omega; \mathbf{r})$ is fixed at $\hat{\chi}$. Because we used a combination of transmitters and receivers, there must be a case where a transmitter is located in the focused receiver. Hence, $\hat{E}^T(\omega; \mathbf{r}_R, \mathbf{r})$ is available in this case. The Green's functions in (9) and (10) offer an accurate propagation model for the assumed heterogeneous background, because $\hat{E}^T(\omega; \mathbf{r}_T, \mathbf{r})$ and $\hat{E}^T(\omega; \mathbf{r}_R, \mathbf{r})$ are optimized in the case with the multilayered medium without including an object. Hence, the enhanced SAR image $\tilde{I}(\mathbf{r})$ is calculated as

$$\tilde{I}(\mathbf{r}) = \sum_{(\mathbf{r}_T, \mathbf{r}_R) \in \Omega_S} \int_{-\infty}^{\infty} \tilde{E}^S(\omega; \mathbf{r}_T, \mathbf{r}_R) \times \tilde{G}_R^B(\omega; \mathbf{r}_R, \mathbf{r}) \tilde{G}_T^{B*}(\omega; \mathbf{r}_T, \mathbf{r}) d\omega \quad (11)$$

where $\tilde{E}^S(\omega; \mathbf{r}_T, \mathbf{r}_R)$ denotes the scattered field defined as $\tilde{E}^S(\omega; \mathbf{r}_T, \mathbf{r}_R) \equiv E^T(\omega; \mathbf{r}_T, \mathbf{r}_R) - \hat{E}^T(\omega; \mathbf{r}_T, \mathbf{r}_R)$,

$\hat{E}^T(\omega; \mathbf{r}_T, \mathbf{r}_R)$ denotes the total field assuming the case with only a background multilayered medium and no object.

Notably, the CSI provides the above total field because CSI outputs the total field in Ω_D and the observation area Ω_S . Thus, once the CSI iteration process is completed assuming the background multilayered media, following the method described in Section IV-A, we can obtain the total field for the background media, namely background clutter responses, $\tilde{E}^S(\omega; \mathbf{r}_T, \mathbf{r}_R)$, as:

$$\begin{aligned} \tilde{E}^S(\omega; \mathbf{r}_T, \mathbf{r}_R) &\equiv E^I(\omega; \mathbf{r}_T, \mathbf{r}_R) \\ &+ k_B^2 \int_{\Omega_D} \tilde{G}_R^{B*}(\omega; \mathbf{r}_R, \mathbf{r}) \tilde{w}(\omega; \mathbf{r}_T, \mathbf{r}) d\mathbf{r} \\ &(\mathbf{r}_R \in \Omega_S) \quad (12) \end{aligned}$$

where $\tilde{G}_R^{B*}(\omega; \mathbf{r}_R, \mathbf{r})$ is obtained in (10). $\tilde{w}(\omega; \mathbf{r}_T, \mathbf{r})$ is defined as $\tilde{w}(\omega; \mathbf{r}_T, \mathbf{r}) \equiv \hat{\chi}(\omega, \mathbf{r}) \hat{E}^T(\omega; \mathbf{r}_T, \mathbf{r})$ where $\hat{\chi}(\omega, \mathbf{r})$ is determined by the optimized contrast function of $\hat{\chi}$ in (8). $\hat{E}^T(\omega; \mathbf{r}_T, \mathbf{r})$ denotes the optimized total field, also used in (9).

C. Procedure of Proposed Method

The procedure of the proposed method is summarized as follows.

- Step 1): The initial estimation of χ is obtained in (8) as $\hat{\chi} \equiv (\chi_1, \dots, \chi_n, \dots, \chi_{N_{\text{layer}}})$.
- Step 2): At a specific angular frequency ω_i , $\hat{E}^T(\omega_i; \mathbf{r}_T, \mathbf{r})$ is optimized by the CSI with fixed $\chi(\omega_i, \mathbf{r})$, derived from $\hat{\chi}$.
- Step 3): The Green's functions $\tilde{G}_T^B(\omega_i; \mathbf{r}_T, \mathbf{r})$ and $\tilde{G}_R^B(\omega_i; \mathbf{r}_R, \mathbf{r})$ are calculated in (9) and (10), respectively, using $\hat{E}^T(\omega_i; \mathbf{r}_T, \mathbf{r})$.
- Step 4): $\tilde{E}^S(\omega_i; \mathbf{r}_T, \mathbf{r}_R)$ is calculated using (12), and the scattered field is determined, assuming multilayered background $\tilde{E}^S(\omega_i; \mathbf{r}_T, \mathbf{r}_R)$.
- Step 5): Steps 2), 3), and 4) are conducted at the number of angular frequency set $\omega \equiv (\omega_1, \dots, \omega_{N_{\text{FR}}})$.
- Step 6): CSI-enhanced SAR images are obtained as $\tilde{I}(\mathbf{r})$ in (11).

Fig. 4 shows the flowchart of the proposed method.

V. RESULTS: FDTD NUMERICAL TEST

A. Numerical Setting

In this section, the 2-D FDTD-based numerical tests are investigated assuming the multilayered ground medium. Fig. 5 shows the two models assumed herein. In this article, here, the multilayered background medium is set in a vacuum, and a set of transmitters and receivers is scanned along the ground surface for $200 \leq x \leq 1800$ mm with 100 mm spacing, namely, monostatic observation model is assumed. We assume the L-band radar and the center frequency and bandwidth of the transmitted raised cosine modulated pulse are 0.58 and 0.37 GHz, respectively. The theoretical range and cross-range resolutions (depth = 40 cm and $\epsilon_B = 6$) are 76 and 53 mm, respectively. The cell sizes for the FDTD and the inversion calculation are set to 10 mm. Table I summarizes the assumed sets of relative permittivity and conductivity for each background layer and buried object. Note that, a number of studies demonstrated that there is no significant frequency

TABLE I
DIELECTRIC PARAMETER FOR EACH LAYER AND OBJECT

	Relative permittivity	Conductivity [S/m]	Dimensions [mm]
Background	1.0	0	-
First Layer	3.0	0.01	1600 mm × 200 mm
Second Layer	6.0	0.1	1600 mm × 200 mm
Third Layer	10.0	1.0	1600 mm × 200 mm
Object	1.0	0	100 mm × 100 mm

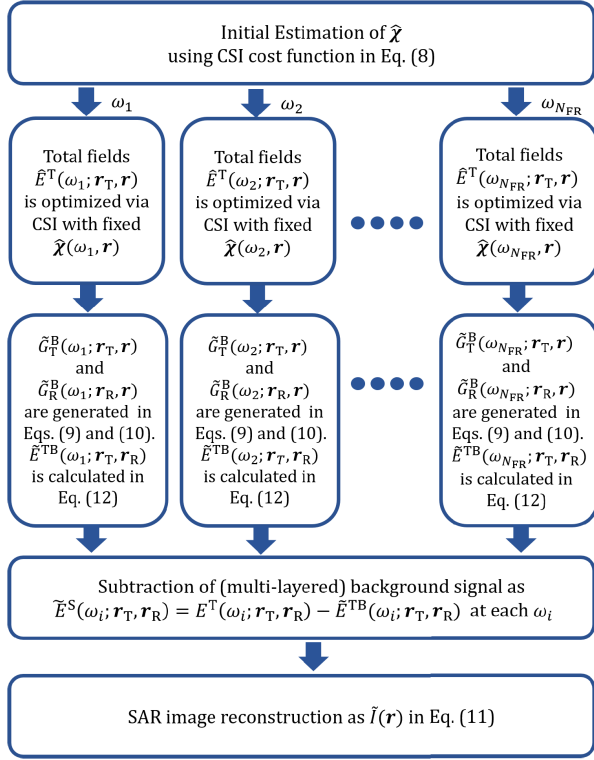


Fig. 4. Processing of the proposed method.

dependency of permittivity in this frequency band [39]. The first, second, and third layers correspond to dry, humid, and saturated clay, respectively. These dielectric values are adopted from the literature [40] at the assumed frequency band. In addition, assuming an air cavity detection under the ground, the buried object is as an air-filled object; each dielectric property was retrieved from the literature [40]. Cases #1 involves a single object in Fig. 5(a) buried at the center of the second layer, and Case #2 involves two objects buried at the first and third layers in Fig. 5(b).

B. Parameters and Conditions

The results of the SAR-based reconstruction for buried objects are obtained as follows. In this test, three conditions of the proposed method are studied to validate the applicability of the CSI-based propagation model. In Conditions I and II, the relative permittivities for each layer are given as true values and are reconstructed using the method [37] in Condition III. Condition I, the total fields $\hat{E}^T(\omega, \mathbf{r}; \mathbf{r}_T)$ and the scattered fields $\tilde{E}^S(\omega; \mathbf{r}_T, \mathbf{r}_R)$ are obtained using the FDTD

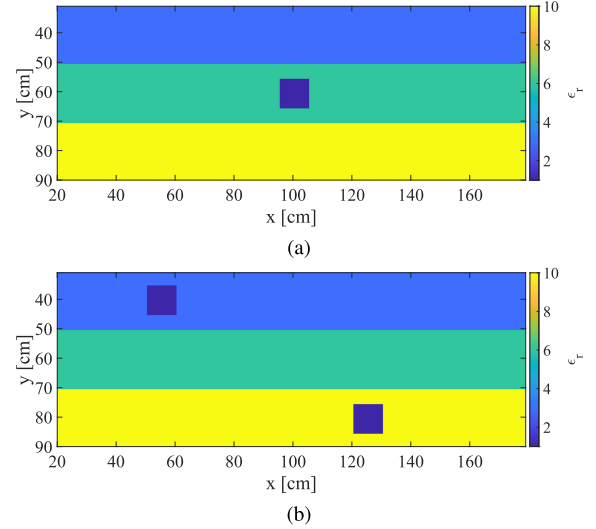


Fig. 5. Ground-truth profiles for relative permittivity of multilayered background medium, including air cavities. (a) Case #1. (b) Case #2.

method; i.e., ideal inputs are available in the enhanced SAR reconstruction. In Conditions II and III, the scattered fields $\tilde{E}^S(\omega; \mathbf{r}_T, \mathbf{r}_R)$ and the total fields $\hat{E}^T(\omega, \mathbf{r}; \mathbf{r}_T)$ are estimated using the CSI. Notably, Condition III is the most practical case when the scattered fields $\tilde{E}^S(\omega; \mathbf{r}_T, \mathbf{r}_R)$ and the total fields $\hat{E}^T(\omega, \mathbf{r}; \mathbf{r}_T)$ are determined by the CSI, where the dielectric constant of each layer is estimated using the method [37] described in Section IV-A. Table II summarizes the above mentioned conditions.

C. Estimations of Dielectric Property in Each Layer

The initial estimation of the dielectric property for each layer is performed using the method described in Section IV-A, where CSI iteration is conducted 2000 times for each combination of $(\epsilon_1, \epsilon_2, \epsilon_3)$ and $\lambda = 900$ in (5) is selected empirically. Fig. 6 shows the distribution of residuals for the cost function, demonstrating that the optimized combination reaches the minimum residual of the CSI cost function around the combinations of $(\epsilon_1, \epsilon_2, \epsilon_3)$. Table III shows the relative permittivity for each layer. The relative permittivities for the first and second layers are accurately provided, while that for the third layer shows some errors. These are due to the insignificant contrast along ϵ_3 of the residual of cost function $\log F$ (Fig. 6). This is because the conductivity of the third layer is relatively higher than that of the other layers, and the radiated electric field cannot penetrate deeply into the third layer. Thus, the response from the bottom

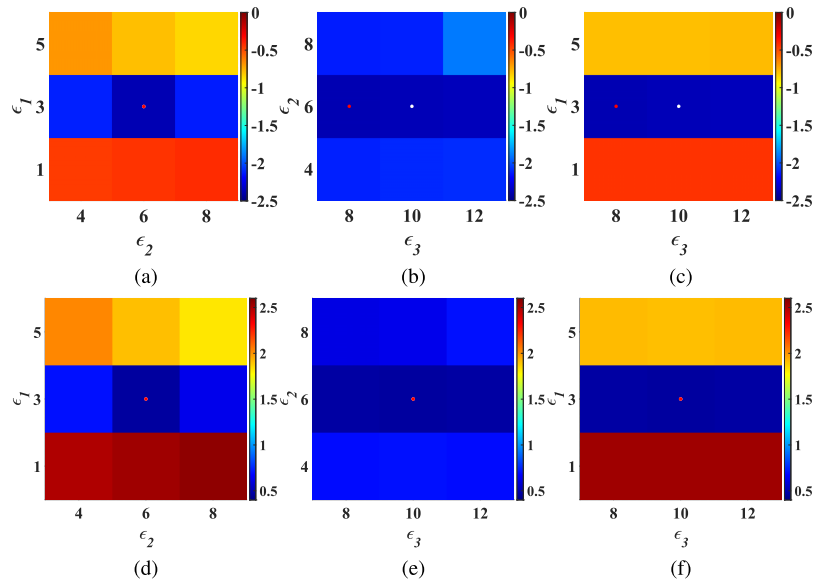


Fig. 6. Cross section profiles of the minimized residual of the cost function in (8) for each combination of relative permittivity. White and red dots denote the true and estimated combination of permittivities, respectively. (a) Case #1 (ϵ_1, ϵ_2). (b) Case #1 (ϵ_2, ϵ_3). (c) Case #1 (ϵ_1, ϵ_3). (d) Case #2 (ϵ_1, ϵ_2). (e) Case #2 (ϵ_2, ϵ_3). (f) Case #2 (ϵ_1, ϵ_3).

TABLE II
DETAILS OF EACH CONDITION OF THE PROPOSED METHOD

	Dielectric constant in each layer	Green's function	Total field of background medium
Condition I	Given	FDTD	FDTD
Condition II	Given	CSI	CSI
Condition III	Method [37]	CSI	CSI

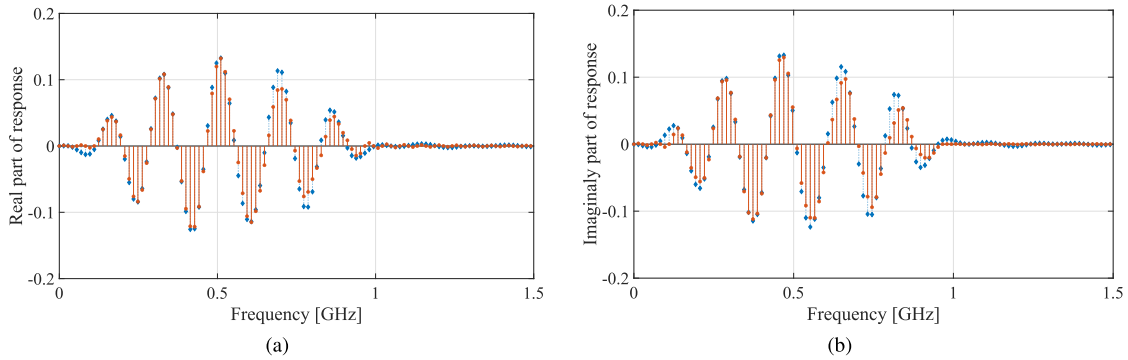


Fig. 7. Reconstruction of the total field at the specific transmitter and the cell in the ROI in the frequency domain. Blue denotes the FDTD data. Red denotes the CSI reconstructed data. (a) Real part. (b) Imaginary part.

TABLE III
RESULTS FOR RELATIVE PERMITTIVITY ESTIMATION
IN EACH CASE USING METHOD [37]

	Case # 1		Case # 2	
	True	Estimated	True	Estimated
# 1	3	3	3	3
# 2	6	6	6	6
# 3	10	8	10	10

of the third layer would be considerably lower, causing a lower contrast of $\log F$, which reflects significantly on the time delay value between each layer. The calculation time is

approximately 117 h for the initial permittivity estimation for each layer, using Intel¹ Xeon¹ Gold 5218 CPU 2.30 GHz with 3.70 TB RAM.

D. Reconstructions of Green's Function and Scattered Field

In the proposed method, the Green's functions defined in (9) and (10) are calculated from the total fields $\hat{E}^T(\omega; \mathbf{r}_T, \mathbf{r})$ and $\hat{E}^T(\omega; \mathbf{r}_R, \mathbf{r})$, which are available from the above minimization procedure using the CSI cost function. The reconstruction results of these total fields are shown in Figs. 7 and 8. These results are also represented in Case #1, where the total fields at

¹Registered trademark.

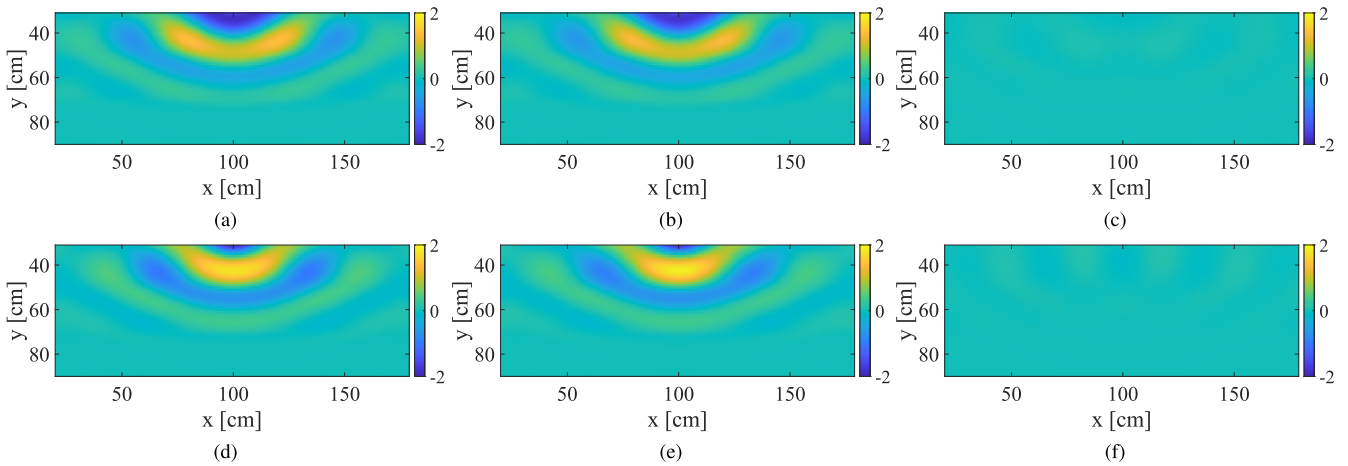


Fig. 8. Real and imaginary values of complex total fields $\hat{E}^T(\omega; \mathbf{r}_T, \mathbf{r})$ at each ROI position by the FDTD (reference) and CSI in Case 3. First line: real part. Second line: imaginary part. (a) and (d) FDTD. (b) and (e) CSI. (c) and (f) Difference.

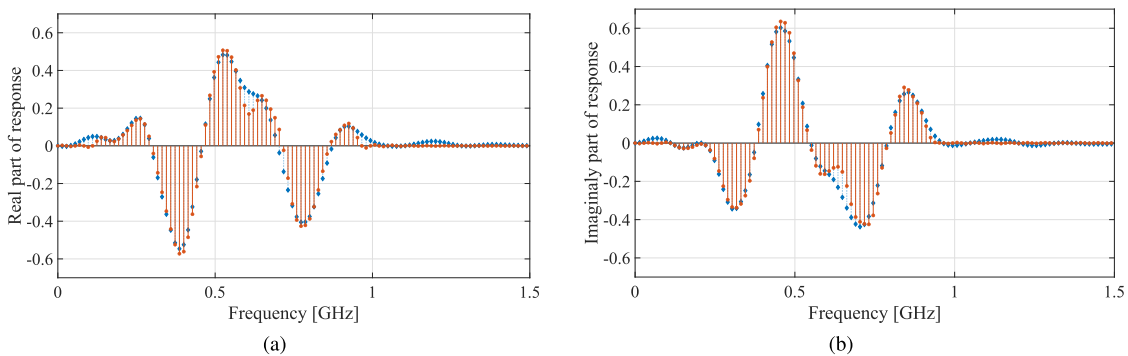


Fig. 9. Reconstruction of the scattered field $\tilde{E}^{TB}(\omega; \mathbf{r}_T, \mathbf{r}_R)$ in (12) at the specific combination of the transmitter and receiver in the ROI, in the frequency domain. Blue denotes the FDTD data. Red denotes the CSI reconstructed data. (a) Real part. (b) Imaginary part.

each ROI position are provided by the FDTD (reference value) and CSI-based optimization in (5). Fig. 7 shows the frequency responses at the specific combination of the transmitter and receiver, and Fig. 8 illustrates the complex value profile of the total fields, at the specific transmitter and frequency at 0.58 GHz. Figs. 7 and 8 demonstrate that the CSI-based total field optimization can reconstruct the total field in all ROI cells and frequency ranges, compared to the FDTD-based reference value, where the difference between FDTD and CSI is significantly smaller than that of maximum values. These results indicate that Green's function can be accurately derived using the proposed CSI approach, assuming a heterogeneous background.

In addition, Fig. 9 shows the results of the reconstruction of the scattered fields $\tilde{E}^{TB}(\omega; \mathbf{r}_T, \mathbf{r}_R)$ in (12), at the specific combination of the transmitter and receiver in the frequency domain. As shown in Fig. 9, the proposed scheme accurately reconstructs the scattered field, that is, the signal including only the buried object. This is because the scattered fields $\tilde{E}^{TB}(\omega; \mathbf{r}_T, \mathbf{r}_R)$ in (12) is determined by only total fields $\hat{E}^T(\omega; \mathbf{r}_T, \mathbf{r})$, which are accurately provided by the CSI as denoted in Fig. 7. This means that a sufficiently accurate estimate of the $E^S(\omega; \mathbf{r}_T, \mathbf{r}_R)$ could be available without using the FDTD forward solvers, which is a distinct advantage of this method over other approaches. Thus, the proposed method

can guarantee the subtraction process between the cases with and without objects.

E. Reconstructions of SAR Based Images

This section presents the image reconstruction results for each method or condition. Regarding Case #1, Fig. 10 shows the reconstruction profiles for the original SAR and the CSI-enhanced SAR (the proposed method) in each target case. In the original SAR scheme, it assumes that three layers have a uniform permittivity, that is, a homogeneous assumption is applied. Here, to assess the dependency on the selected relative permittivities, the three different relative permittivities are given as 3, 6, and 9, which are transformed to propagation velocity utilized in (2) and (3) as $c_B = c_{\text{air}}/\sqrt{\epsilon_B}$. In addition, to distinguish the second advantage of the proposed method, that is, the clutter elimination scheme employing the CSI output, the two conditions for the original SAR are introduced. The first condition is that the scattered field designated as $\tilde{E}^{TB}(\omega; \mathbf{r}_T, \mathbf{r}_R)$, is provided by the FDTD, implying that background clutter from each layer is completely eliminated, which is denoted as “w/ complete clutter suppression” in Fig. 10(a)–(c). Note that, such a condition is hardly available in real-world situation. Further, i.e., a more practical scenario entails suppressing only the reflection from the first layer,

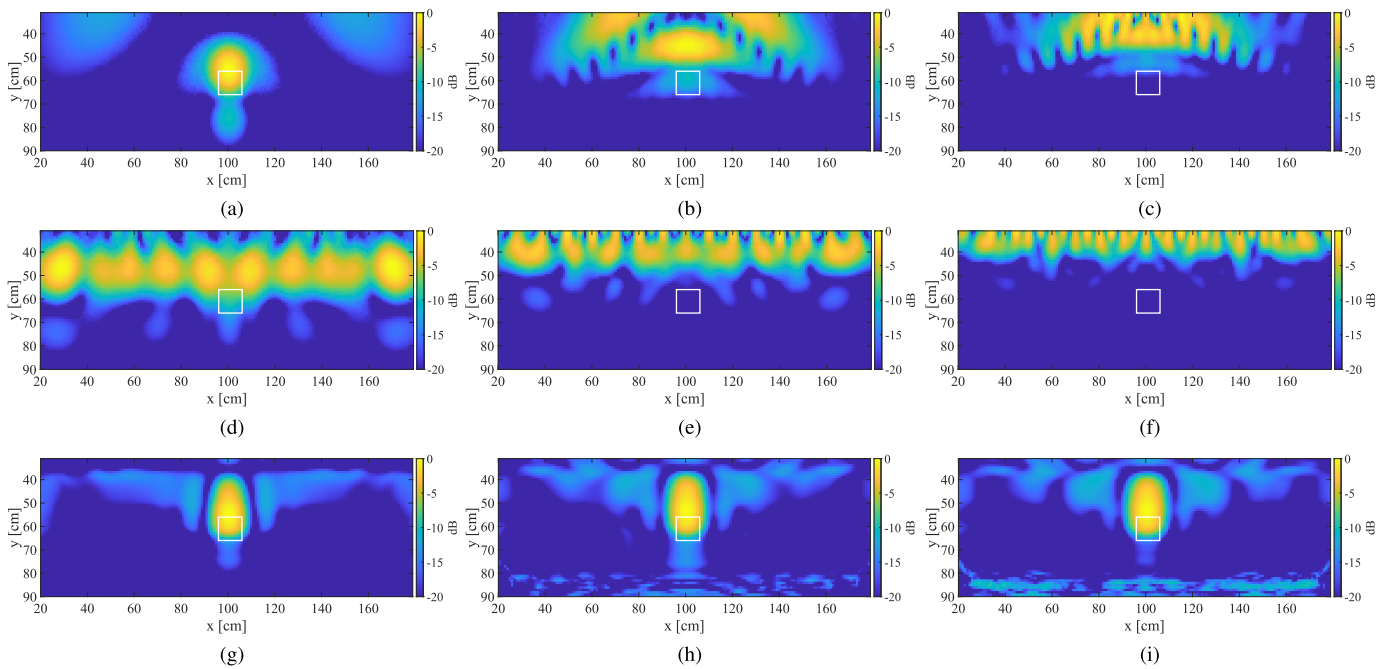


Fig. 10. Reconstruction DAS images in the Case #1. White rectangular line denotes the actual boundary of buried object. Color denotes the magnitude of the image. (a) Conventional SAR ($\epsilon_B = 3$) w/ complete clutter suppression. (b) Conventional SAR ($\epsilon_B = 6$) w/ complete clutter suppression. (c) Conventional SAR ($\epsilon_B = 9$) w/ complete clutter suppression. (d) Conventional SAR ($\epsilon_B = 3$) w/ only first layer surface clutter suppression. (e) Conventional SAR ($\epsilon_B = 6$) w/ only first layer surface clutter suppression. (f) Conventional SAR ($\epsilon_B = 9$) w/ only first layer surface clutter suppression. (g) Proposed (Condition I). (h) Proposed (Condition II). (i) Proposed (Condition III).

which is indicated as “w/ only the first layer surface complete clutter suppression” as shown in Fig. 10(d)–(f). Because the clutter response from the first layer is mostly dominating and readily reduced by applying average signal subtraction or window-based filtering for shallow areas, this situation is frequently used in many GPR applications [41], [42]. Notably, it is extremely difficult to eliminate the clutter signals from the second or deeper layers because the object may be located at the same depth as these deeper layers or may possess a shape similar to that of a planar layer. Focusing on the original SAR with complete clutter suppression, even if the background clutter is perfectly suppressed, it cannot appropriately locate the buried object position, especially in the case of $\epsilon_B = 6$ and 9 because the original SAR considers the homogeneous background medium. The cases in $\epsilon_B = 3$ provide relatively accurate profiles because they match the relative permittivity of the first layer. However, the above parameter could not be determined without prior knowledge of the target depth or the permittivity of each layer. The first inherent problem with the original SAR is that its accuracy depends highly on the selected dielectric contrasts ϵ_B . In addition, in the second condition, that is, w/ only first layer surface complete clutter suppression, the original SAR severely suffers from unnecessary responses, which are mainly caused by the reflection responses between first and second layers. Therefore, an accurate clutter suppression scheme for deeper layers is required. However, to the best of our knowledge, the implementation of such schemes has not been achieved in any existing studies, posing a significant obstacle to the standard SAR approach.

On the contrary, the reconstruction image by the proposed method accurately focuses on the location of the actual buried object in any condition. Condition I uses the FDTD based referential data using the Green’s function and the total fields of background medium as $\tilde{E}^{TB}(\omega; \mathbf{r}_T, \mathbf{r}_R)$. Subsequently, the accurate propagation for multilayer background generates a reliable image with clutter free signals. Notably, while Conditions II and III do not employ the above knowledge, but use the CSI optimized outputs, the proposed schemes retain the accurate target reconstruction image (that is almost the same as that assumed in Condition I) by eliminating the false images occurring in the original SAR image. This is because the Green’s function and $\tilde{E}^{TB}(\omega; \mathbf{r}_T, \mathbf{r}_R)$ could be accurately reconstructed in the CSI approach, as demonstrated in Section V-D. In addition, the second flaw in the original SAR approach, an insufficient clutter suppression, is efficiently addressed by referring to Conditions II or III in the proposed method, which uses the CSI outputs for clutter signal generation. Furthermore, in Condition III, the dielectric constant of the third layer is not correctly given, the reconstruction image still offers accurate target position, because the target is located at second layer, and the accuracy for the propagation model into the third layer is not significantly affected. Note that, the focused image even in using accurate Green’s function in the proposed method does not place on the center of the buried target but on the upper boundary of the object. This is due to the reflection signal being from the object’s upper boundary, which is caused by the dielectric difference between the background medium and the object (air). that is an essential and inherent characteristic of SAR imaging.

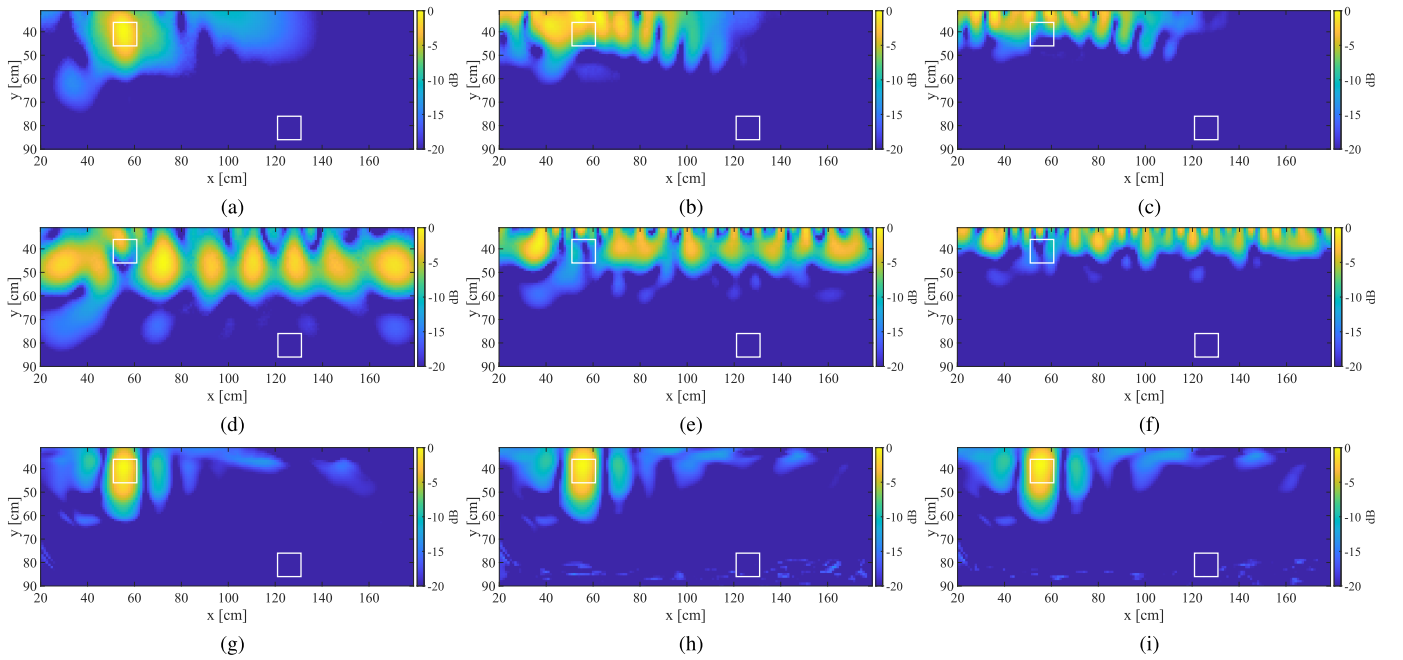


Fig. 11. Reconstruction DAS images in the Case #2. White rectangular line denotes the actual boundary of buried object. Color denotes the magnitude of the image. (a) Conventional SAR ($\epsilon_B = 3$) w/ complete clutter suppression. (b) Conventional SAR ($\epsilon_B = 6$) w/ complete clutter suppression. (c) Conventional SAR ($\epsilon_B = 9$) w/ complete clutter suppression. (d) Conventional SAR ($\epsilon_B = 3$) w/ only first layer surface clutter suppression. (e) Conventional SAR ($\epsilon_B = 6$) w/ only first layer surface clutter suppression. (f) Conventional SAR ($\epsilon_B = 9$) w/ only first layer surface clutter suppression. (g) Proposed (Condition I). (h) Proposed (Condition II). (i) Proposed (Condition III).

Second, focusing on the Case #2, the results for each method are shown in Fig. 11 and are similar to those in Case #1. The original SAR suffers from image distortions owing to inappropriate selection of the relative permittivity of background ϵ_B , even in the case with complete clutter suppression. In addition, the insufficient clutter reduction results in non-negligible unwanted responses as in Fig. 11(d)–(f). On the contrary, the proposed method retains its accuracy in each condition. However, in both cases, the object buried in the third layer could not be shown in each method or case. This is because the object is buried in the layer with high conductivity and generates a weaker echo than the object buried in the first layer. This is a limitation of both methods, and should be resolved using an attenuation compensation approach [43], [44].

Regarding the quantitative analysis of reconstruction images, we introduce three criteria for the obtained images, signal-to-mean ratio (SMR), signal-to-clutter ratio (SCR), and the location errors of the target (Err_{loc}). The SCR is the power ratio from the first maximum peak to the second maximum peak of an image and assesses the clutter suppression ratio. The SMR is the power ratio from the first maximum peak to the average strength of the ROI. These two criteria have been widely accepted in evaluating SAR-based images [45], [46]. As another metric focusing on the peak position of each image, the following error is defined:

$$\text{Err}_{\text{loc}} = \|\mathbf{p}_{\text{true}} - \hat{\mathbf{p}}_{\text{CI}}\| \quad (13)$$

where \mathbf{p}_{true} denotes the true position of the object, defined as the center of the upper surface of the object. $\hat{\mathbf{p}}_{\text{CI}}$ expresses

the position with a maximum response of each image. Tables IV and V show the SMR, SCR, and Err_{loc} in each method for Case #1 and #2, respectively. These tables demonstrate that compared to the values obtained by conventional SAR images, the proposed approach retains a higher SMR or SCR value and a lower Err_{loc} value in both cases.

F. Case With Additive Noise

We next investigate the sensitivity to additive noise for each method as follows. The white Gaussian noises are added to each scattered signal in the time domain. The signal-to-noise ratio (SNR) is defined as the ratio of maximum signal power to noise variance, where the signal represents the reflection responses from multilayer medium, which is considerably stronger than that from the buried object. We assume the representative case as 30 dB SNR. Fig. 12 shows the example of reflection responses without or with subtraction for three-layered background responses in this case. Note that, when we consider that the signal power is only from the buried object as shown in Fig. 12(b), its SNR is from 0 to 10 dB, which would be available in a real scenario demonstrated in [47] and [8]. Case #1 is assumed, and Fig. 13 shows the distribution of CSI cost functions' residual for each permittivity combination in (5), and it also demonstrated that the optimal solution reaches to the actual combination even in this noisy scenario, indicating the noise-robustness for permittivity estimation using (5). In addition, Fig. 14 depicts the reconstruction outcomes using each approach under various settings. Because the conventional or proposed SAR technique can minimize noise components due to coherent

TABLE IV
QUANTITATIVE IMAGE EVALUATIONS IN EACH METHOD AT CASE #1

Method	Conventional SAR w/ complete clutter suppression			Conventional SAR w first layer surface clutter suppression			Proposed Method		
	$\epsilon_B = 3$	$\epsilon_B = 6$	$\epsilon_B = 9$	$\epsilon_B = 3$	$\epsilon_B = 6$	$\epsilon_B = 9$	Condition I	Condition II	Condition III
SCR	23.0 dB	0.2 dB	0.1 dB	0.0 dB	0.8 dB	0.0 dB	27.3 dB	26.2 dB	20.6 dB
SMR	44.9 dB	35.6 dB	40.4 dB	25.6 dB	34.9 dB	42.0 dB	48.4 dB	42.5 dB	42.0 dB
Err _{loc}	10 mm	110 mm	283 mm	717 mm	472 mm	292 mm	10 mm	30 mm	32 mm

TABLE V
QUANTITATIVE IMAGE EVALUATIONS IN EACH METHOD AT CASE #2

Method	Conventional SAR w/ complete clutter suppression			Conventional SAR w first layer surface clutter suppression			Proposed Method		
	$\epsilon_B = 3$	$\epsilon_B = 6$	$\epsilon_B = 9$	$\epsilon_B = 3$	$\epsilon_B = 6$	$\epsilon_B = 9$	Condition I	Condition II	Condition III
SCR	14.8 dB	0.1 dB	0.7 dB	2.9 dB	0.8 dB	2.0 dB	19.6 dB	19.4 dB	20.0 dB
SMR	45.1 dB	40.9 dB	49.1 dB	26.8 dB	37.0 dB	44.2 dB	49.8 dB	46.8 dB	47.6 dB
Err _{loc}	41 mm	82 mm	196 mm	19.2 mm	50 mm	304 mm	32 mm	32 mm	22 mm

TABLE VI
QUANTITATIVE IMAGE EVALUATIONS IN EACH METHOD AT CASE #1 AT SNR = 30 dB

Method	Conventional SAR w/ complete clutter suppression			Proposed Method		
	$\epsilon_B = 3$	$\epsilon_B = 6$	$\epsilon_B = 9$	Condition I	Condition II	Condition III
SCR	15.5 dB	4.9 dB	1.0 dB	23.9 dB	18.8 dB	18.8 dB
SMR	39.2 dB	31.8 dB	31.6 dB	43.9 dB	38.9 dB	38.9 dB
Err _{loc}	10 mm	149 mm	243 mm	20 mm	32 mm	32 mm

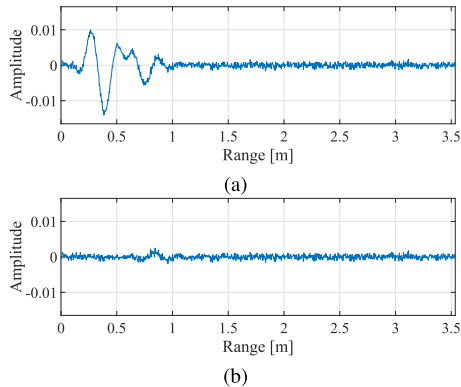


Fig. 12. Examples of reflection responses without and with subtraction of three-layer background medium at the SNR of 30 dB case. (a) W/o subtraction. (b) W/ subtraction.

integration effects, these figures illustrate that our proposed method greatly preserves reconstruction accuracy even in such low SNR cases. Table VI also shows the quantitative image evaluations in this case, and this table also demonstrates that our proposed method retains the same SCR, SMR, or error level assuming the noise-free case.

G. Case With Heterogeneous Layer Model

Furthermore, to assess the applicability for the practical scenario, the heterogeneous layer model is investigated as follows. While the previous model assumes that each layer has a fully homogeneous medium, there should be variations

in permittivity and conductivity for each layer. Fig. 15 shows the heterogeneous profiles for permittivity and conductivity using the above model. Here to generate a heterogeneous layer model, a certain level of variations for permittivity and conductivity are given using the Gaussian distribution. In particular, for permittivity and conductivity, we add the random fluctuations generated by a normal distribution with a fixed standard deviation to each layer parameter as $(\sigma_{\epsilon,1}, \sigma_{\epsilon,2}, \sigma_{\epsilon,3}) = (0.6, 1.2, 2.0)$ and $(\sigma_{\sigma,1}, \sigma_{\sigma,2}, \sigma_{\sigma,3}) = (0.002, 0.02, 0.2 \text{ S/m})$, respectively, where $\sigma_{\epsilon,i}$ and $(\sigma_{\sigma,i})$ denote the standard deviations at the i th layer for permittivity and conductivity, respectively, that are 20% of the assumed permittivity and conductivity at each layer. And then, these profiles are smoothed using the Gaussian filter with the correlation length $\sigma_{GSS} = 50 \text{ mm}$. Table VII shows the permittivity estimation results for each layer in this situation, demonstrating that the approach [37] would still offer a valid estimate for the #1 and #2 layers, which are the same as Table III's homogeneous case. Fig. 16 shows the reconstruction results in this case for each method. As demonstrated by these data, both the traditional and proposed approaches have non-negligible unnecessary responses produced by the heterogeneity of each layer model. Since the proposed method calculates Green's function assuming a homogeneous multilayer model, it could not completely suppress the clutter responses due to heterogeneity in each layer in (12). Table VIII also shows the quantitative evaluations in this case, and it demonstrates that our proposed method improves the SCR ratio marginally, which would be due to a more accurate Green's function. Nonetheless, more research is

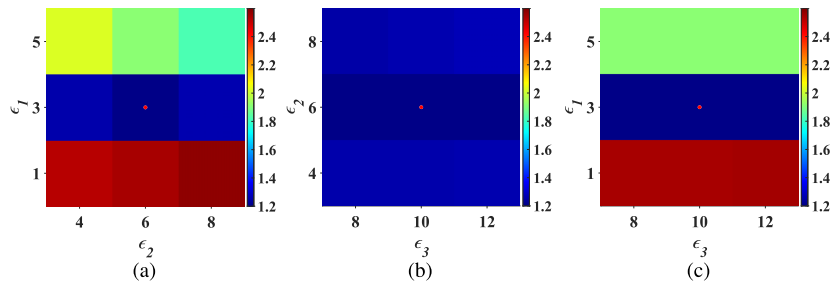


Fig. 13. Cross section profiles of the minimized residual of the cost function in (8) for each combination of relative permittivity at SNR of 30 dB. White and red dots denote the true and estimated combination of permittivities, respectively. (a) Case #1 (ϵ_1, ϵ_2). (b) Case #1 (ϵ_2, ϵ_3). (c) Case #1 (ϵ_1, ϵ_3).

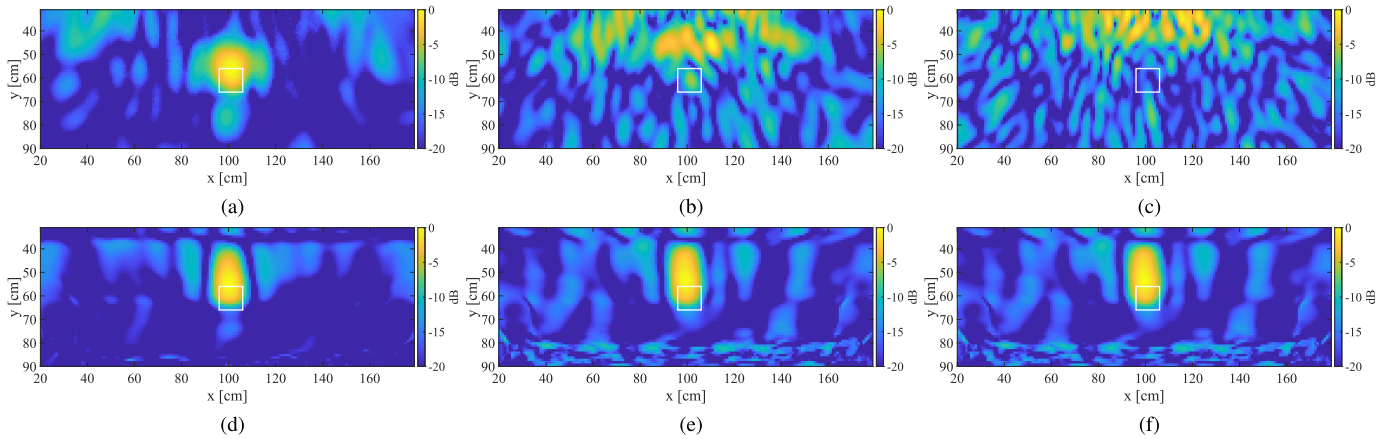


Fig. 14. Reconstruction DAS images in the Case #1 at the case for SNR = 30 dB. White rectangular line denotes the actual boundary of buried object. Color denotes the magnitude of the image. (a) Conventional SAR ($\epsilon_B = 3$) w/ complete clutter suppression. (b) Conventional SAR ($\epsilon_B = 6$) w/ complete clutter suppression. (c) Conventional SAR ($\epsilon_B = 9$) w/ complete clutter suppression. (d) Proposed (Condition I). (e) Proposed (Condition II). (f) Proposed (Condition III).

TABLE VII
RESULTS FOR RELATIVE PERMITTIVITY ESTIMATION IN EACH CASE USING METHOD [37] AT HETEROGENEOUS LAYER MODEL SHOWN IN FIG. 15

	# 1	# 2	# 3
True	3	6	10
Estimated	3	6	8

needed to solve the aforementioned heterogeneity model, such as reconstructing a dielectric profile with more unknowns to offer an accurate background dielectric profile in the proposed method.

H. Computational Complexity

The computational complexity for each approach is investigated as follows. Table IX summarizes the computational complexity and actual run time, using the computational resources using Intel Xeon Gold 5218 CPU 2.30 GHz and 3.70 TB RAM. Here, as described in Section V-A, N_{FR} is the number of frequency samples. N_{layer} is the number of layers, and N_{scan} is the number of scanning points. N_{SMP} denotes the number of sampling points of ϵ_i . N_{ROI} is the number of cells in the ROI, and N_{ite} is the number of iterations required in the CSI. Initially, the total computational time for the relative permittivity estimation by the method [37] is

approximately 100 h, where $N_{FR} = 10$, $N_{scan} = 17$, $N_{layer} = 3$, $N_{SMP} = 3$, $N_{ROI} = 9600$, and $N_{ite} = 2000$ are set. This process requires large computational complexity, however, if we obtain prior knowledge or a rough estimation of the permittivity of each layer, the “Index 2” process could be omitted. There are several promising approaches for obtaining the relative permittivity for each layer [48], [49]. While the conventional DAS process requires limited computational time (“Index 1”), compared with those required in the proposed method as Index 3, 4, and 5. the complexities of Index 4 and 5 are the same as that of Index 1, namely, the homogeneous-based SAR approach. The Index 3 process depends highly on the iteration number of the CSI (N_{ite}), where $N_{ite} = 1000$ is set. However, this value could be reduced using a more appropriate initial estimate from the pre-process in Index 2. In addition, there are some studies assuming a multilayer medium [35], which is predicted to be of lower complexity using geometrical optics (GO) approximation based on Green’s function. However, those approaches basically do not include a clutter suppression scheme and do or not account for diffraction or multiple scattering effects between numerous layers, resulting in reconstruction inaccuracy due to unwanted responses of the aforementioned clutters. Nonetheless, it is our important future work to reduce an actual run time, by eliminating redundant processing or introducing an under-sampling scheme such as for total-field optimization in the CSI.

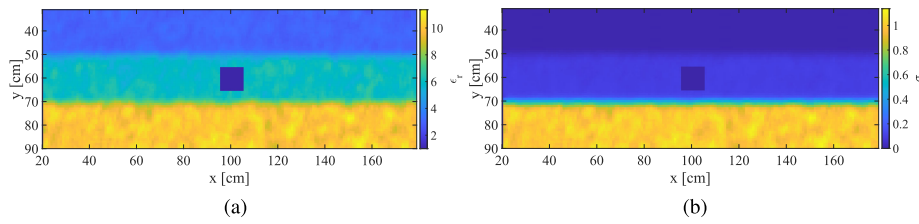


Fig. 15. Ground truth profiles for relative permittivity of heterogeneous multilayered background medium, including air cavities. (a) Relative permittivity. (b) Conductivity.

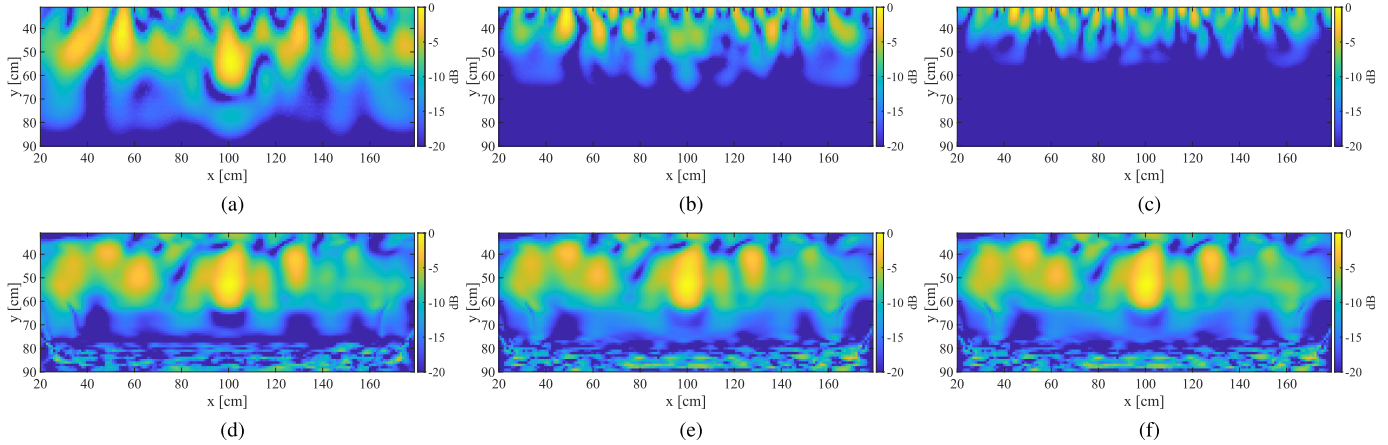


Fig. 16. Reconstruction DAS images at the heterogeneous layer model shown in Fig. 15. White rectangular line denotes the actual boundary of buried object. Color denotes the magnitude of the image. (a) Conventional SAR ($\epsilon_B = 3$) w/ complete clutter suppression. (b) Conventional SAR ($\epsilon_B = 6$) w/ complete clutter suppression. (c) Conventional SAR ($\epsilon_B = 9$) w/ complete clutter suppression. (d) Proposed (Condition I). (e) Proposed (Condition II). (f) Proposed (Condition III).

TABLE VIII
QUANTITATIVE IMAGE EVALUATIONS IN EACH METHOD FOR HETEROGENEOUS MODEL AT CASE #1

Method	Conventional SAR w/ complete clutter suppression			Proposed Method		
	$\epsilon_B = 3$	$\epsilon_B = 6$	$\epsilon_B = 9$	Condition I	Condition II	Condition III
SCR	0.0 dB	3.6 dB	1.6 dB	2.9 dB	5.1 dB	5.8 dB
SMR	24.5 dB	37.6 dB	44.9 dB	24.7 dB	25.4 dB	25.0 dB
Err_{loc}	22 mm	552 mm	604 mm	30 mm	30 mm	30 mm

TABLE IX
COMPUTATIONAL COMPLEXITY AND ACTUAL RUN TIME IN EACH PROCESS

Index		Complexity	Run time
1	Conventional SAR processing in Eq. (1)	$O(N_{\text{scan}}N_{\text{ROI}}N_{\text{FR}})$	0.25 s
2	Permittivity estimation by Method [37]	$O(N_{\text{scan}}N_{\text{SMP}}^{N_{\text{layer}}}N_{\text{ROI}}N_{\text{FR}}N_{\text{ite}})$	6000 min
3	Optimization of total fields by CSI	$O(N_{\text{scan}}N_{\text{ROI}}N_{\text{FR}}N_{\text{ite}})$	180 min
4	Process in Eq. (9), Eq. (10), and (12)	$O(N_{\text{scan}}N_{\text{ROI}}N_{\text{FR}})$	110 s
5	Proposed SAR processing in Eq. (11)	$O(N_{\text{scan}}N_{\text{ROI}}N_{\text{FR}})$	5 s

I. Limitations and Further Discussions

This section clarifies the limitations of the proposed method, assuming the realistic scenario. To begin, the proposed method requires prior knowledge of the number of layers, whereas the standard SAR methodology does not, and there may be circumstances where the aforesaid information is missing or provided incorrectly. While many studies stated that the number of layers could be obtained by evaluating the down

range profile of B-scan data [50], it should be noted that the selection of layer number in the proposed method would affect the final reconstruction outcomes. To demonstrate the above point, we introduced the validations in the scenario that the number of layers is wrongly given. First, we assume the Case #1 model, which has three layers as illustrated in Fig. 5(a), but we give an inappropriate assumption as two layers model as shown in Fig. 17 in the proposed method, where each layer has a thickness of 300 mm and dielectric

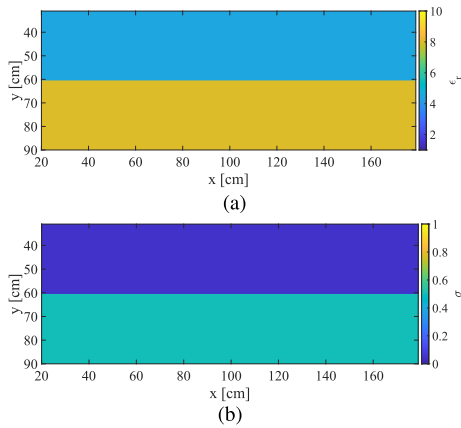


Fig. 17. Assumed profiles of relative permittivity and conductivity in two layers model for Case #1, in the proposed method. (a) Relative permittivity. (b) Conductivity.

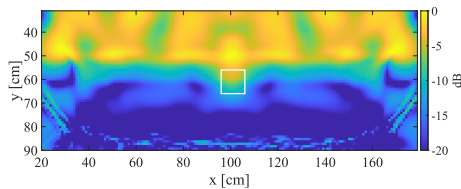


Fig. 18. Reconstruction DAS images in the Case #1 by the proposed method, using the inappropriate assumption of the number of layers as two layer model. White rectangular line denotes the actual boundary of buried object. Color denotes the magnitude of the image. (a) Proposed (Condition I).

properties of $(\epsilon, \sigma) = (4.5, 0.05 \text{ S/m})$ for the first layer and $(\epsilon, \sigma) = (8.0, 0.5 \text{ S/m})$ for the second layer, which are intermediate values for the three layers model, Case #1, as shown in Fig. 5(a). In this situation, the above false assumption likely to have an effect on the reconstruction accuracy of Green's functions or background clutter production in the proposed method given in Section IV-B. Fig. 18 depicts the reconstruction results obtained by the proposed method with Condition I, demonstrating that there are numerous unnecessary responses in the upper layer area, owing to insufficient clutter reduction in (12), because the total field $E^T(\omega; \mathbf{r}_T, \mathbf{r})$ in the ROI is generated by the two-layer models. The Green's functions used in (11) is also miscalculated by the above total fields in (9) and (10), which focuses the scattered signals on the upper side of the actual target boundary. Then, the prior knowledge of the number of layers and thickness are critical, and that is the limitation of the proposed method. However, assuming a general GPR scenario, some studies could provide the number of layers from B-scan data [51], or using other measurement techniques such as ultrasound. Thus, the combination used for the above approaches should be included as the pre-processing scheme in a realistic situation.

VI. CONCLUSION

Herein, we presented an inverse scattering-enhanced radar imaging technique for ground-penetrating or general subsurface imaging scenarios using low-frequency band microwave. The proposed technique is mainly divided into the two steps. In the first step, the initial estimate of the background multiple layers is performed by assessing the minimum residual of

the CSI cost function based on a previous study [37], which can massively reduce the computational cost. In the second step, the propagation model in the assumed heterogeneous multilayer background is accurately estimated by the total fields of ROI cells, optimized by the CSI scheme in the first step. Notably, the proposed method newly focusing on the CSI optimization approach, can provide an accurate initial estimate of relative permittivity and numerous total fields optimized on each ROI cell, facilitating the calculation of an appropriate Green's function. In addition, the total fields from background media can be provided by the CSI outputs, namely, the Green's function and the contrast profile of the background, enabling us to eliminate the clutter components such as multiple reflections between layers. By exploiting the above feature, the accuracy of radar images, such as SAR, can be remarkably upgraded compared to the traditional SAR approach using average permittivity for the propagation model in a multilayered model.

Assuming different subsurface scenarios using the L-band signal, the numerical 2-D FDTD test demonstrates that our proposed method considerably enhances the reconstruction accuracy, especially for the multilayered background with high contrasts. Furthermore, while the traditional DAS approach suffers from critical false images due to the reflection among layers, the proposed method completely suppresses these clutter responses using Green's function, which can compensate for the single or multiple reflection effects among the background layers. Notably, the proposed method can be applied to low and high contrast multilayer models because the Green's function or clutter suppression can be generated using the CSI scheme. In particular, when assuming higher dielectric contrast layers, the convergence speed of CSI may decrease owing to high nonlinearity. However, the aforementioned concern can be alleviated by providing an appropriate initial dielectric contrast during the process described in Section IV-A. In addition, in lower contrast cases, such as those close to homogeneous backgrounds, the proposed method is not necessarily required to enhance the reconstruction accuracy. However, an initial estimate of the average permittivity of the layers is required for SAR processing. While no experimental validations are offered in this study, our proposed methodology appears to be a potential solution for conventional GRP imaging problems, particularly in multilayered subsurface scenarios. Furthermore, by including an appropriate inverse scattering analysis, such as [29], the proposed approach would provide a significant estimate for the post-quantitative reconstruction of dielectric property for buried objects.

REFERENCES

- [1] Japan Ministry of Land, Infrastructure, Transport and Tourism, Council for Social Infrastructure Development. Accessed: Dec. 13, 2020. [Online]. Available: https://www.mlit.go.jp/policy/shingikai/kanbo08_sg_000106.html
- [2] C. Özdemir, F. Demirci, E. YiLit, and B. Yilmaz, "A review on migration methods in B-scan ground penetrating radar imaging," *Math. Problems Eng.*, vol. 13, pp. 1607–1620, Jul. 1997.
- [3] N. Smitha, D. R. U. Bharadwaj, S. Abilash, S. N. Sridhara, and V. Singh, "Kirchhoff and F-K migration to focus ground penetrating radar images," *Int. J. Geo-Eng.*, vol. 7, no. 1, p. 4, Dec. 2016.

- [4] M. González-Díaz, M. García-Fernández, Y. Álvarez-López, and F. Las-Heras, "Improvement of GPR SAR-based techniques for accurate detection and imaging of buried objects," *IEEE Trans. Instrum. Meas.*, vol. 69, no. 6, pp. 3126–3138, Jun. 2020.
- [5] J. I. Halman, K. A. Shubert, and G. T. Ruck, "SAR processing of ground-penetrating radar data for buried UXO detection: Results from a surface-based system," *IEEE Trans. Antennas Propag.*, vol. 46, no. 7, pp. 1023–1027, Jul. 1998.
- [6] M. Fallahpour, J. T. Case, M. T. Ghasr, and R. Zoughi, "Piecewise and Wiener filter-based SAR techniques for monostatic microwave imaging of layered structures," *IEEE Trans. Antennas Propag.*, vol. 62, no. 1, pp. 282–294, Jan. 2014.
- [7] G. Wang, C. Ma, and J. Jiang, "On ground penetrating radar imaging method based on compressed sensing in multi-target environment," in *Proc. Chin. Control Conf. (CCC)*, Guangzhou, China, Jul. 2019, pp. 3332–3336.
- [8] J. Li, C. Le Bastard, Y. Wang, G. Wei, B. Ma, and M. Sun, "Enhanced GPR signal for layered media time-delay estimation in low-SNR scenario," *IEEE Geosci. Remote Sens. Lett.*, vol. 13, no. 3, pp. 299–303, Mar. 2016.
- [9] W. C. Chew and Y. M. Wang, "Reconstruction of two-dimensional permittivity distribution using the distorted born iterative method," *IEEE Trans. Med. Imag.*, vol. 9, no. 2, pp. 218–225, Jun. 1990.
- [10] D. W. Winters, B. D. Van Veen, and S. C. Hagness, "A sparsity regularization approach to the electromagnetic inverse scattering problem," *IEEE Trans. Antennas Propag.*, vol. 58, no. 1, pp. 145–154, Jan. 2010.
- [11] E. Pettinelli et al., "GPR response from buried pipes: Measurement on field site and tomographic reconstructions," *IEEE Trans. Geosci. Remote Sens.*, vol. 47, no. 8, pp. 2639–2645, Aug. 2009.
- [12] F. Soldovieri, J. Hugenschmidt, R. Persico, and G. Leone, "A linear inverse scattering algorithm for realistic GPR applications," *Near Surf. Geophysics*, vol. 5, no. 1, pp. 29–41, Feb. 2007.
- [13] G. Leone and F. Soldovieri, "Analysis of the distorted born approximation for subsurface reconstruction: Truncation and uncertainties effects," *IEEE Trans. Geosci. Remote Sens.*, vol. 41, no. 1, pp. 66–74, Jan. 2003.
- [14] P. M. V. D. Berg and R. E. Kleinman, "A contrast source inversion method," *Inverse Problems*, vol. 13, no. 6, pp. 1607–1620, Dec. 1997.
- [15] P. M. V. D. Berg, A. L. V. Broekhoven, and A. Abubakar, "Extended contrast source inversion," *Inverse Problems*, vol. 15, no. 5, pp. 1325–1344, Oct. 1999.
- [16] P. M. van den Berg, A. Abubakar, and J. T. Fokkema, "Multiplicative regularization for contrast profile inversion," *Radio Sci.*, vol. 38, no. 2, pp. 23-1–23-10, Apr. 2003.
- [17] N. Anselmi, L. Poli, G. Oliveri, and A. Massa, "Iterative multiresolution Bayesian CS for microwave imaging," *IEEE Trans. Antennas Propag.*, vol. 66, no. 7, pp. 3665–3677, Jul. 2018.
- [18] M. Salucci et al., "A multi-resolution computational method to solve highly non-linear inverse scattering problems," *J. Phys., Conf. Ser.*, vol. 1476, May 2020, Art. no. 012002.
- [19] M. Salucci, L. Poli, N. Anselmi, and A. Massa, "Multifrequency particle swarm optimization for enhanced multiresolution GPR microwave imaging," *IEEE Trans. Geosci. Remote Sens.*, vol. 55, no. 3, pp. 1305–1317, Mar. 2017.
- [20] G. Oliveri, Y. Zhong, X. Chen, and A. Massa, "Multiresolution subspace-based optimization method for inverse scattering problems," *J. Opt. Soc. Amer. A, Opt. Image Sci.*, vol. 28, no. 10, pp. 2057–2069, Oct. 2011.
- [21] X. Ye et al., "Multi-resolution subspace-based optimization method for solving three-dimensional inverse scattering problems," *J. Opt. Soc. Amer. A, Opt. Image Sci.*, vol. 32, pp. 2218–2226, Nov. 2015.
- [22] G. Oliveri, L. Poli, and A. Massa, "On the exploitation of the a-priori information through the Bayesian compressive sensing for microwave imaging," in *Proc. 6th Eur. Conf. Antennas Propag. (EUCAP)*, Mar. 2012, pp. 1502–1503.
- [23] M. Salucci, L. Tenuti, G. Oliveri, and A. Massa, "Frequency-hopping GPR prospecting of sparse scatterers through Bayesian compressive sensing," in *Proc. Int. Appl. Comput. Electromagn. Soc. Symp. Italy (ACES)*, Mar. 2017, pp. 1–2.
- [24] L. Tenuti, M. Salucci, L. Poli, G. Oliveri, and A. Massa, "Physical-information exploitation in inverse scattering approaches for GPR survey," in *Proc. 9th Eur. Conf. Antennas Propag. (EuCAP)*, Apr. 2015, pp. 1–4.
- [25] S. Sun, B. J. Kooij, and A. G. Yarovoy, "Linearized 3-D electromagnetic contrast source inversion and its applications to half-space configurations," *IEEE Trans. Geosci. Remote Sens.*, vol. 55, no. 6, pp. 3475–3487, Jun. 2017.
- [26] R. Marklein, J. Miao, M. Rhaman, and K. J. Langenberg, "Inverse scattering and imaging in NDT: Recent applications and advances," in *Proc. Conf., 9th Eur. Conf. NDT*, Sep. 2006, pp. 1–8.
- [27] L.-P. Song, Q. Huo Liu, F. Li, and Z. Qing Zhang, "Reconstruction of three-dimensional objects in layered media: Numerical experiments," *IEEE Trans. Antennas Propag.*, vol. 53, no. 4, pp. 1556–1561, Apr. 2005.
- [28] M. A. Ali and M. Moghaddam, "3D nonlinear super-resolution microwave inversion technique using time-domain data," *IEEE Trans. Antennas Propag.*, vol. 58, no. 7, pp. 2327–2336, Jul. 2010.
- [29] S. Takahashi, K. Suzuki, T. Hanabusa, and S. Kidera, "Microwave subsurface imaging method by incorporating radar and tomographic approaches," *IEEE Trans. Antennas Propag.*, vol. 70, no. 11, pp. 11009–11023, Nov. 2022.
- [30] S. Takahashi and S. Kidera, "Incorporation algorithm with RPM and DBIM in Bayesian framework for microwave non-destructive testing," in *Proc. URSI Asia-Pacific Radio Sci. Conf. (AP-RASC)*, Mar. 2019, pp. 1–4.
- [31] M. Benedetti, M. Donelli, D. Lesselier, and A. Massa, "A two-step inverse scattering procedure for the qualitative imaging of homogeneous cracks in known host media—preliminary results," *IEEE Antennas Wireless Propag. Lett.*, vol. 6, pp. 592–595, 2007.
- [32] O. Dorn and D. Lesselier, "Level set methods for inverse scattering," *Inverse Problems*, vol. 22, no. 4, pp. R67–R131, Aug. 2006.
- [33] H. Sato and S. Kidera, "ROI limited unknowns reduction-based contrast source inversion for microwave breast imaging," *IEEE Antennas Wireless Propag. Lett.*, vol. 19, no. 12, pp. 2285–2289, Dec. 2020.
- [34] M. Salucci, L. Poli, N. Anselmi, and A. Massa, "Multi-scale compressive processing for inverse scattering within the contrast source formulation," in *Proc. IEEE Int. Symp. Antennas Propag. USNC-URSI Radio Sci. Meeting*, Jul. 2019, pp. 1017–1018.
- [35] W. Zhang and A. Hoorfar, "MIMO ground penetrating radar imaging through multilayered subsurface using total variation minimization," *IEEE Trans. Geosci. Remote Sens.*, vol. 57, no. 4, pp. 2107–2115, Apr. 2019.
- [36] G. Umezū, Y. Yamauchi, and S. Kidera, "Contrast source inversion enhanced confocal imaging for highly heterogeneous breast media in microwave mammography," *IEEE J. Electromagn., RF Microw. Med. Biol.*, vol. 6, no. 4, pp. 494–500, Dec. 2022.
- [37] Y. Yamauchi and S. Kidera, "Contrast source inversion for objects buried into multi-layered media for subsurface imaging applications," *IEICE Trans. Electron.*, vol. E106.C, no. 7, pp. 427–431, 2023.
- [38] Y. Yamauchi and S. Kidera, "Inverse scattering enhanced synthetic aperture imaging for multi-layered ground media," in *Proc. Int. Symp. Antennas Propag. (ISAP)*, Sydney, NSW, Australia, Oct. 2022, pp. 225–226.
- [39] J. B. Paknahad, K. Sheshyekani, F. Rachidi, M. Paolone, and A. Mimouni, "Evaluation of lightning-induced currents on cables buried in a lossy dispersive ground," *IEEE Trans. Electromagn. Compat.*, vol. 56, no. 6, pp. 1522–1529, Dec. 2014.
- [40] J. B. Rhebergen, H. A. Lensen, P. B. W. Schwering, G. R. Marín, and J. M. H. Hendrickx, "Soil moisture distribution around land mines and the effect on relative permittivity," in *Proc. SPIE*, Aug. 2002, Art. no. 479098.
- [41] X. Wei and Y. Zhang, "Interference removal for autofocusing of GPR data from RC bridge decks," *IEEE J. Sel. Topics Appl. Earth Observ. Remote Sens.*, vol. 8, no. 3, pp. 1145–1151, Mar. 2015.
- [42] E. Temlioglu and I. Erer, "Clutter removal in ground-penetrating radar images using morphological component analysis," *IEEE Geosci. Remote Sens. Lett.*, vol. 13, no. 12, pp. 1802–1806, Dec. 2016.
- [43] K. Feng, Y. Zhao, Z. Zhang, and S. Ge, "Stratigraphic absorption compensation of GPR signal based on improved S-transform," in *Proc. 8th Int. Workshop Adv. Ground Penetrating Radar (IWAGPR)*, Jul. 2015, pp. 1–4.
- [44] P. X. Neto and W. E. de Medeiros, "A practical approach to correct attenuation effects in GPR data," *J. Appl. Geophys.*, vol. 59, no. 2, pp. 140–151, Jun. 2006.
- [45] H. Song et al., "Detectability of breast tumors in excised breast tissues of total mastectomy by IR-UWB-radar-based breast cancer detector," *IEEE Trans. Biomed. Eng.*, vol. 66, no. 8, pp. 2296–2305, Aug. 2019.
- [46] D. Ireland and M. Bialkowski, "Microwave head imaging for stroke detection," *Prog. Electromagn. Res. M*, vol. 21, pp. 163–175, Oct. 2011.
- [47] J. Zhang, S. Ye, Y. Lin, X. Liu, and G. Fang, "A modified model for quasi-monostatic ground penetrating radar," *IEEE Geosci. Remote Sens. Lett.*, vol. 17, no. 3, pp. 406–410, Mar. 2020.

- [48] C.-S. Lee and C.-L. Yang, "Thickness and permittivity measurement in multi-layered dielectric structures using complementary split-ring resonators," *IEEE Sensors J.*, vol. 14, no. 3, pp. 695–700, Mar. 2014.
- [49] H. Liu, K. Takahashi, and M. Sato, "Measurement of dielectric permittivity and thickness of snow and ice on a brackish lagoon using GPR," *IEEE J. Sel. Topics Appl. Earth Observ. Remote Sens.*, vol. 7, no. 3, pp. 820–827, Mar. 2014.
- [50] K. Ren, J. Chen, and R. J. Burkholder, "A 3-D uniform diffraction tomographic algorithm for near-field microwave imaging through stratified media," *IEEE Trans. Antennas Propag.*, vol. 66, no. 6, pp. 3034–3045, Jun. 2018.
- [51] L. Qu, Q. Sun, T. Yang, L. Zhang, and Y. Sun, "Time-delay estimation for ground penetrating radar using ESPRIT with improved spatial SmoothingTechnique," *IEEE Geosci. Remote Sens. Lett.*, vol. 11, no. 8, pp. 1315–1319, Aug. 2014.



Yoshihiro Yamauchi received the B.E. degree in communication engineering and informatics and the M.E. degree in informatics and communication engineering from the University of Electro-Communications, Tokyo, Japan, in 2021 and 2023, respectively.

He joined Capgemini Japan K.K., Tokyo, in 2023.



Shouhei Kidera (Senior Member, IEEE) received the B.E. degree in electrical and electronic engineering and the M.I. and Ph.D. degrees in informatics from Kyoto University, Kyoto, Japan, in 2003, 2005, and 2007, respectively.

In 2009, he joined as an Assistant Professor with the University of Electro-Communications, Tokyo, Japan, where he is currently a Full Professor with the Graduate School of Informatics and Engineering. He stayed at the Cross-Disciplinary Electromagnetics Laboratory, University of Wisconsin–Madison, Madison, WI, USA, as a Visiting Researcher, in 2016. He was a Principal Investigator of the PRESTO Program, Japan Science and Technology Agency (JST), Tokyo, from 2017 to 2021. His current research interests include advanced radar signal processing or electromagnetic inverse scattering issue for ultra-wideband (UWB) 3-D sensor or biomedical applications.

Dr. Kidera is a Senior Member of the Institute of Electronics, Information, and Communication Engineers of Japan (IEICE), and the International Union of Radio Science (Union Radio-Scientifique Internationale, URSI), and a member of the Institute of Electrical Engineering of Japan (IEEJ), and the Japan Society of Applied Physics (JSAP). He was a recipient of the 2012 Ando Incentive Prize for the Study of Electronics, the 2013 Young Scientist's Prize by the Japanese Minister of Education, Culture, Sports, Science and Technology (MEXT), the 2014 Funai Achievement Award, the 2022 KDDI Foundation Award, the Contribution Award, and the 2023 RIEC Award.